nature photonics

ARTICLES

PUBLISHED ONLINE: 13 JUNE 2016 | DOI: 10.1038/NPHOTON.2016.104

Phase-locked laser arrays through global antenna mutual coupling

Tsung-Yu Kao[1,2], John L. Reno[3] and Qing Hu[1]*

Phase locking of an array of lasers is a highly effective method in beam shaping because it increases the output power and reduces the lasing threshold. Here, we show a conceptually novel phase-locking mechanism based on 'antenna mutual coupling' in which laser elements interact through far-field radiations with definite phase relations. This allows a long-range global coupling among the array elements to achieve a robust phase locking in two-dimensional laser arrays. The scheme is ideal for lasers with a deep subwavelength confined cavity, such as nanolasers, whose divergent beam patterns could be used to achieve a strong coupling among the elements in the array. We demonstrated experimentally such a scheme based on subwavelength short-cavity surface-emitting lasers at terahertz frequencies. More than 37 laser elements that span over ~8 λ_o were phase locked to each other, and delivered up to 6.5 mW (in a pulsed operation) single-mode radiation at ~3 THz, with a maximum 450 mW A^{-1} slope efficiency and a near-diffraction-limited beam divergence.

Phase locking of an array of lasers is a highly effective way to combine coherently the output radiations from individual lasers to achieve beam shaping and a higher output power. Moreover, the interaction between array elements could lead to a significant reduction in the lasing threshold. Recently, a new genre of laser cavity with deep subwavelength confinement in two or three dimensions, such as nanolasers or spasers[1–3] and photonic wire lasers[4], has found various potential applications in fields such as optical-information processing, short-distance communication between integrated circuits and optical sensing[5]. However, substantial developments in reducing the excess lasing threshold and improving the coupling of light into a well-defined free-space mode are still required before these devices can be truly useful. If the phase-locking technique could be properly applied here, it will be a key method to overcome the aforementioned shortcomings.

A robust phase locking requires strong couplings among the individual lasers so that otherwise-independent oscillators are forced to oscillate in sync. Currently, there are four demonstrated coupling schemes to phase-lock integrated diode laser arrays—laser ridges are coupled through exponentially decaying fields outside the high refractive-index dielectric core (evanescent-wave coupled[6]) or through the Talbot feedback from external reflectors (diffraction-wave coupled[7,8]), or by connecting two ridges to one single-mode waveguide (Y-coupled[9,10]) or through lateral propagating waves (Leaky-wave coupled[11–13]). Here we present a novel coupling scheme for phase-locking 2D laser arrays through 'global antenna mutual coupling'. This scheme is distinctly different from the other two phase-locking mechanisms for non-contacting laser elements. In contrast to the evanescent-wave coupled scheme, in which the coupling is through near-field electromagnetic fields, as in the antenna mutual coupled scheme, the coupling is established between two laser elements through far-field radiations with definite phase relations. This allows long-range (many wavelengths in free space) global coupling among the array elements. In contrast with the diffraction-wave coupled scheme, the phase-locking mechanism presented here does not require any external feedback components. The proposed scheme is especially suitable for lasers with deep subwavelength dimensions with divergent radiation beams[14] that could be utilized to achieve a strong coupling among individual lasers in the array.

In this demonstration, we chose short-cavity surface-emitting terahertz (10^{12} hertz) quantum cascade lasers (QCLs)[15–17] in metal–metal waveguides[18]. For the free-space wavelength $\lambda_o \approx 100$ μm, with typical cavity dimensions of 10 μm in thickness, 10–15 μm in width and 30–40 μm in total cavity length, the laser elements clearly fall under the category of a deep subwavelength confined system. A terahertz QCL system was chosen for a less-stringent fabrication requirement at relatively long wavelengths. As electromagnetic waves are scalable, the result presented here can be applied to other frequency ranges by simply scaling the dimensions.

For a deep subwavelength confined laser, because the laser waveguide is smaller than the wavelength, the subwavelength facet of the laser can be modelled as a special type of electromagnetic emitter known as the 'slot antenna'[19]. From antenna theory, each emitter is not only determined by the internal drive, but it is also affected by the radiations from other emitters. This coupling between two electromagnetic emitters can be characterized quantitatively by the mutual admittance, defined as $G_{M(i,j)} = (\text{current})_i/(\text{voltage})_j$, where indices i and j are designated for different emitters. The far-field approximation of mutual admittance, G_M, between two slot antennas with the same electric-field amplitude, width W and height $d \ll W$ placed on an infinite ground plane (x–y plane) can be calculated using equation (1)[20]. Referring to the geometry shown in Fig. 1a, the mutual admittance between two slot antennas that radiate into the upper half space can be written as:

$$G_M = \frac{1}{\pi}\sqrt{\frac{\epsilon}{\mu}}\int_0^{\pi} \frac{\sin^2\left(\frac{\pi W}{\lambda_0}\cos\theta\right)}{\cos^2\theta}\sin^3\theta \times J_0\left(\frac{y}{\lambda_0}2\pi\sin\theta\right)\cos\left(\frac{x}{\lambda_0}2\pi\cos\theta\right)\mathrm{d}\theta \quad (1)$$

[1]Department of Electrical Engineering and Computer Science and Research Laboratory of Electronics, Massachusetts Institute of Technology, Cambridge, Massachusetts 02139, USA. [2]LongWave Photonics LLC, Mountain View, California 94043, USA. [3]Sandia National Laboratories, Center of Integrated Nanotechnologies, MS 1303, Albuquerque, New Mexico 87185-130, USA. *e-mail: qhu@mit.edu

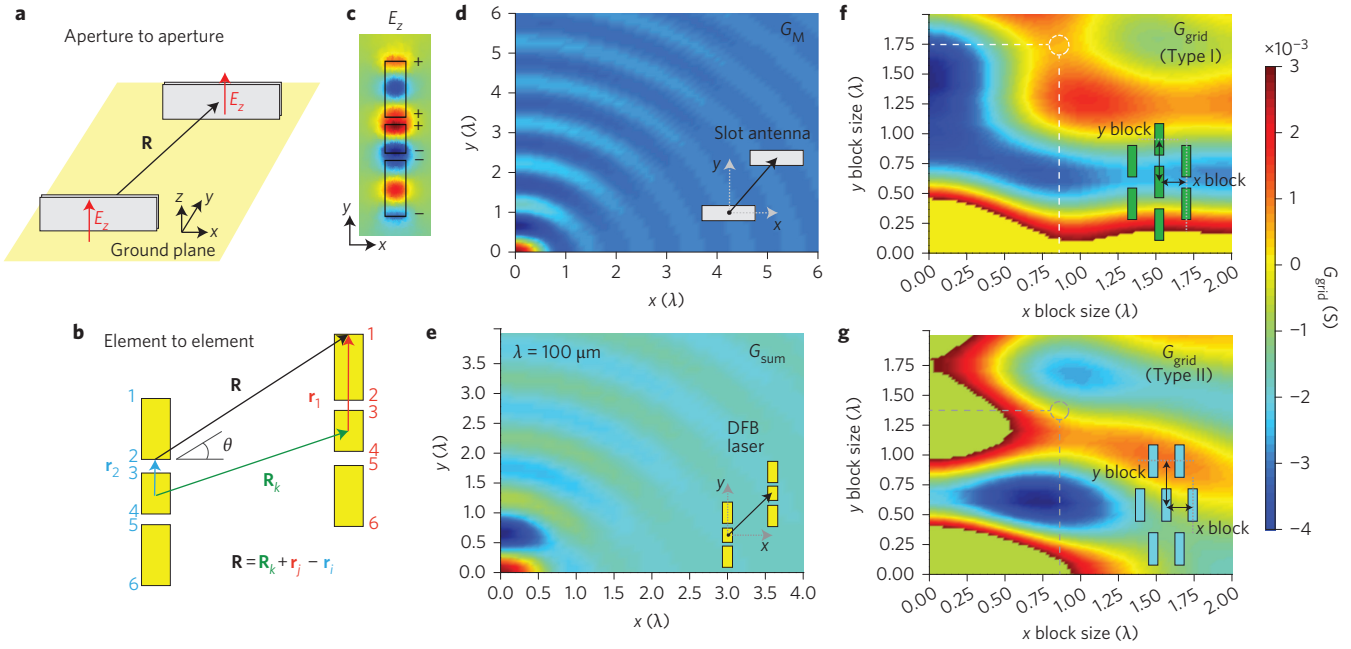

Figure 1 | Mutual admittance and electric-field distribution of the QCL. a,**b**, Schematic for calculating two slot antennas on an infinite ground plane (assuming the direction normal to the slot antenna facet is along the *y* direction and one of the slot antenna is placed at the origin) (**a**) and two three-section surface-emitting DFB lasers (top view) (**b**). $\theta \equiv \arctan(y/x)$. **c**, The electric-field distribution inside the three-section second-order DFB laser when operated in the surface-emitting mode. The relative polarity of each facet is also shown as (+1, +1, +1, –1, –1, –1). The change in polarity sign is the desired outcome of the centre π shift, which is introduced to obtain single-lobe beam patterns from the surface-emitting laser[28]. The longer section is 32 μm in length ($\sim\lambda_S$) with a 4.5 μm gap size. The length of the short centre cavity is 16 μm ($\sim\lambda_S/2$) and the ridge width is 15 μm. **d**, Mutual admittance G_M between two slot antennas calculated using equation (1). **e**, Mutual admittance G_{sum} between two three-section DFB lasers by summing the mutual admittances between slots. **f**,**g**, The sum of all mutual admittances, G_{grid}, from other elements in the array under a Type I grid (**f**), and the G_{grid} for a Type II grid (**g**). Only the nearest-neighbour contributions are included in this simulation. The width of the slot is $W = 15$ μm with a wavelength of $\lambda_0 = 100$ μm. The element is the three-section DFB laser shown in **c**. The *x*–*y* coordinates are normalized to the free-space wavelength λ_0. Certain sets of grid sizes are marked with dotted lines as a visual aid.

where J_0 is the zeroth-order Bessel function of the first kind, ε and μ are the electromagnetic permittivity and permeability, respectively, λ_o is the free-space wavelength, x and y are the position of the second slot and $\theta \equiv \arctan(y/x)$. G_M is plotted along the x–y plane in Fig. 1d. The sign of G_M depends on the relative polarity of the slot antenna pair.

In the investigation of phase locking, emission measurements in the direction normal to the arrays were performed. Thus, we chose a second-order distributed feedback laser (DFB) structure for the laser element. To enhance the array effect, we used the simplest second-order DFB structure, which included only one λ_s (wavelength in the semiconductor) in each end of a π shifter. The overall three-section structure consists of six different slots from the front and rear facets of each section. When two such identical laser elements have their centre positions displaced by $\mathbf{R}_k$ on the x–y plane, the total mutual admittances between the two lasers can be calculated by summing the mutual admittances between all the slot–slot pairs (Fig. 1b). The summation of the mutual admittances is:

$$G_{sum}(\mathbf{R}_k) \equiv \sum_j \sum_i A_{ij}\, G_M\left(\mathbf{R}_k + \mathbf{r}_j - \mathbf{r}_i\right) \quad (2)$$

where i and j are dummy indices for different slots in the same DFB laser and $\mathbf{r}_i$ and $\mathbf{r}_j$ are the relative displacement vectors from the centre of each DFB laser to the position of each slot. $A_{ij} \equiv A_i \times A_j$ is the coefficient of relative polarities and amplitudes for slot i and slot j on different DFB lasers. Figure 1e shows the mutual admittance between two three-section second-order DFB lasers calculated using equation (2). To simplify the calculation, we assume the field at each slot aperture to be identical in amplitude.

When more DFB lasers are arranged to form a 2D grid, for each element in the grid the total mutual admittance contributed by all the other elements (G_{grid}) can be calculated using equation (3):

$$G_{grid} \equiv \sum_k \left(B_k G_{sum}(\mathbf{R}_k)\right) \quad (3)$$

where $\mathbf{R}_k$ includes all the possible lattice vectors given the grid type and B_k determines the relative phase and magnitude of each DFB laser. When $B_k = 1$ for all k, every element in the array is in-phase coupled with an equal field magnitude. Figure 1f shows G_{grid} for a 'Type I' grid under different distances between the elements (see the inset for the definitions). Figure 1g shows G_{grid} for another grid configuration, 'Type II'. The computed mutual admittance sensitively depends on the grid geometry between the elements. In essence, a large positive value of G_{grid} corresponds to a reduction of the radiation resistance, which reduces the radiation loss of the array structure and consequently lowers the lasing threshold. This simplified simulation shows that by choosing an appropriate set of grid geometry, one can increase or decrease the mutual admittance seen by each emitter and, as a result, enhance or suppress specific spatial modes.

To take into account all the possible spatial modes that exist in the laser array system, 3D full-wave finite element method (FEM) quasi-eigenmode simulations were carried out for laser arrays that consisted of three-section second-order DFB lasers with different numbers of elements in the array at different grid sizes. From the simulation, one can find the optimum geometry in which the desired mode has the lowest threshold among all the spatial modes, and thus becomes the lasing mode (see 'Laser array design method' section in the Supplementary Information for a

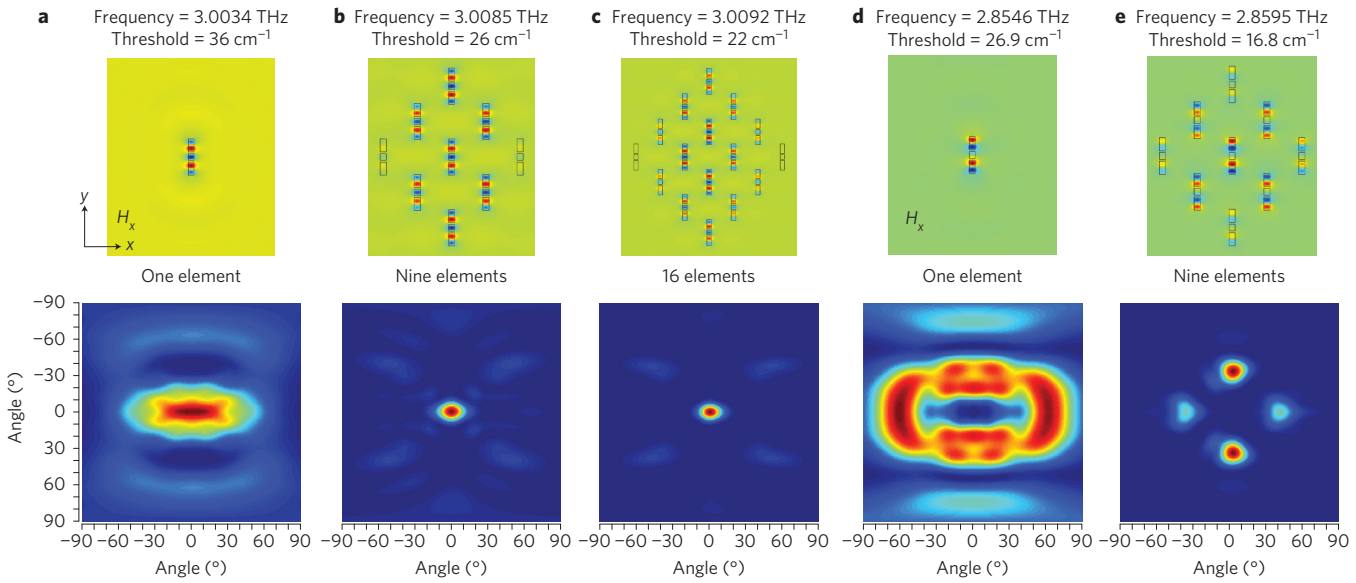

Figure 2 | Magnetic (*H*) fields inside the laser cavity and far-field beam patterns from 3D FEM simulations. a–c, A single three-section second-order DFB laser (**a**), a nine-element array of three-section DFB lasers (**b**) and a 16-element array of DFB lasers (**c**) under a Type I grid with *x* block size = 85 μm and *y* block size = 175 μm. The single-lobe beam divergence reduces with an increasing number of elements in the array. **d**,**e**, Simulated magnetic fields inside the laser cavity and far-field beam patterns for the high-order longitudinal mode of a single three-section DFB laser (**d**) and a nine-element array of DFB lasers (**e**). Although the beam divergence also reduces with an increasing number of elements in the array, a beam pattern of multiple lobes is clearly shown.

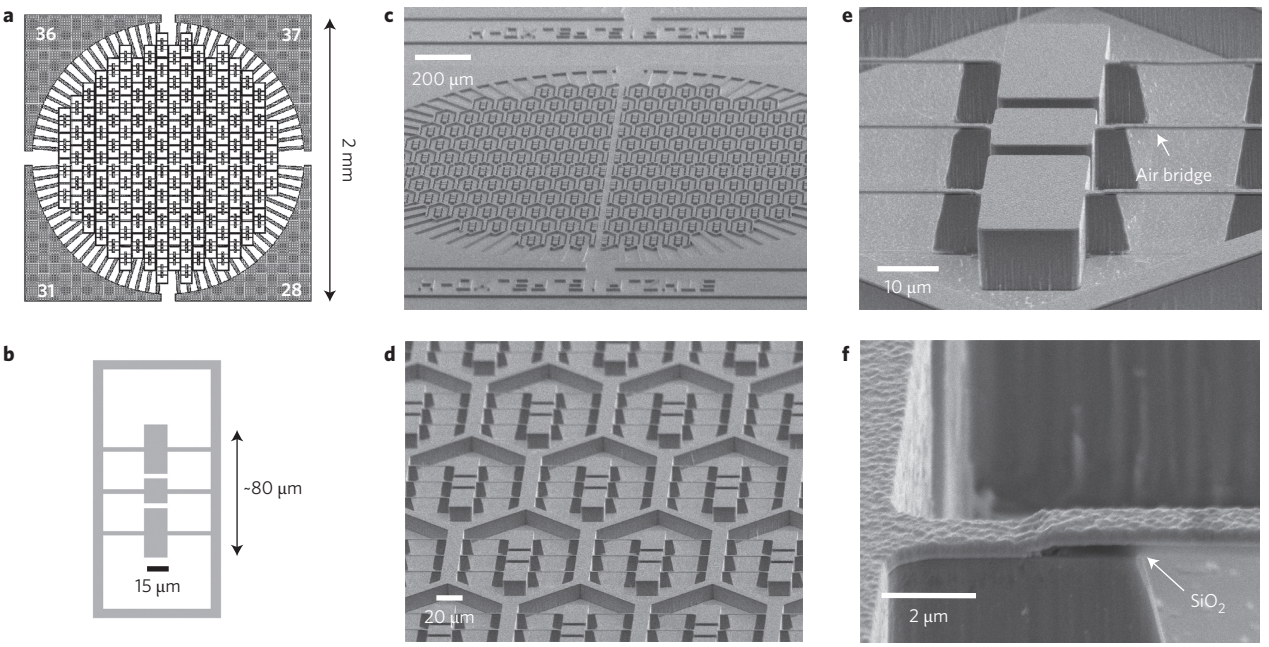

Figure 3 | The laser arrays. a, Schematic of coupled laser arrays with the three-section DFB laser as the building element. The outer dimension is 2 mm and the diameter of the inner circle is ~1.7 mm. The laser array is separated into four subparts for biasing in each quadrant individually. The bonding pads are also shown. The number marked on each pad indicates the total number of the elements electrically connected by each bonding pad. **b**, Schematic of a three-section surface-emitting second-order DFB laser. **c–f**, SEM pictures of the antenna mutual-coupled laser array arranged in a Type II grid. **c**, The overall view of the laser array. The vertical cut in the centre on the biasing rims that separates the laser array into four quadrants is clearly seen at this angle. **d**, Close-up view of the grid configuration. **e**, Single-element three-section DFB laser. The laser consists of three segments: one short half-wavelength centre cavity and two one-wavelength cavities on both sides. The current is provided to the laser through the metal contact on the air-bridge structure. **f**, Close-up view of one end of the air-bridge structure. The dielectric with a dark shade beneath the metal contact is an electrical insulation layer formed by SiO_2.

more detailed conclusion). Figure 2 shows the simulated magnetic fields of a single-element DFB laser, a nine-element laser array and a 16-element laser array with the Type I grid. When the correct sets of grid dimensions are used, the spatial mode with the lowest lasing threshold will be the in-phase mode, as shown in Fig. 2b,c. The far-field beam patterns from the in-phase mode show a significant reduction in divergence when more elements are added to the array. The lasing threshold (which is only caused by radiation loss) of the laser array drops from ~36 cm^{-1} for the single-element laser to ~22 cm^{-1} for the 16-element array. The reduction

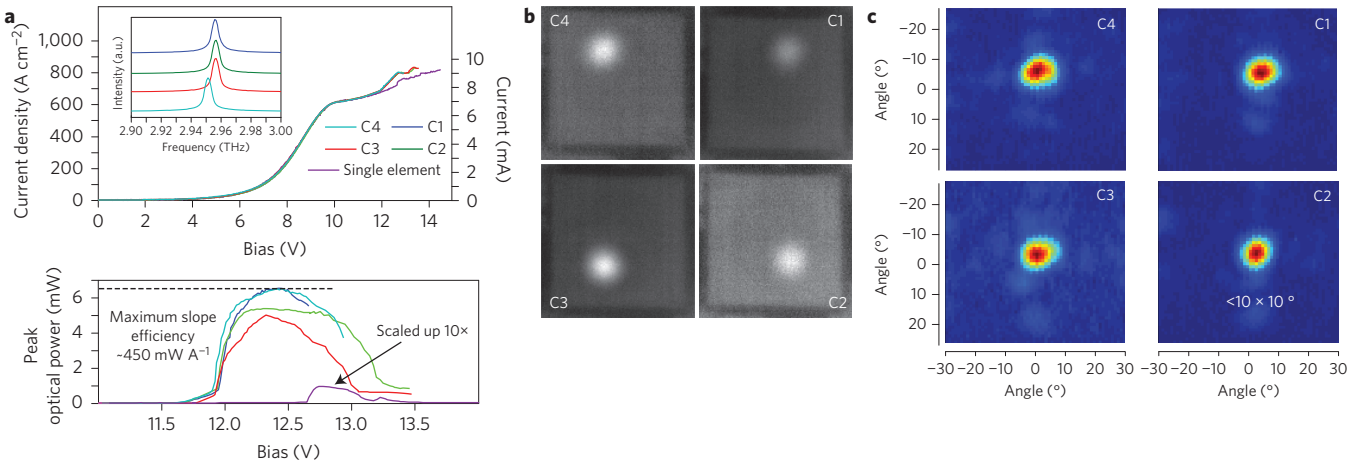

Figure 4 | The four quadrants of the laser array. a, Pulsed *I*–*V* curves (top), *L*–*V* curves (bottom) and lasing spectra (pulsed; inset in top panel) from different quadrants on laser array Chip No. 27. The measurement from a single-element three-section DFB laser is also shown after scaling up the power axis. From the *L*–*V* curves, a clear change in the lasing thresholds between the single-element laser and the phased-locked laser array can be observed. Current flowing through a single-element device is labelled on the axis on the right-hand side (top), from which one can infer the total current by multiplying the current by the number of array elements. All the quadrants show single-mode emission when C1, C2 and C3 lase at the same frequency. The emission frequency of C4 is slightly red shifted from those of the other three quadrants, which probably results from fabrication variation or post-fabrication contamination. The resolution of the FTIR spectrometer is 0.125 cm^{-1}. The laser array in C1 delivers 6.5 mW peak power (black dashed line) with a maximum ~450 mW A^{-1} slope efficiency (bottom). **b**, Terahertz images of the emission from the laser array when different quadrants are biased. The images show narrow single-lobe symmetric terahertz emissions from the laser arrays. The lasers are only biased slightly above the lasing threshold to prevent the terahertz emissions from saturating the camera, so that the outline of the laser array chip could be visible in the images. **c**, Far-field beam patterns from different quadrants of the phase-locked laser arrays measured using a pyroelectric detector located ~20 cm away from the laser array and mechanically scanned over ±30° in both horizontal and vertical directions.

in the lasing threshold (radiation loss) can be attributed to the fact that more electromagnetic energy is now used to establish mutual coupling rather than radiating into the far field. The selected x block size (85 μm ≈ 0.85 λ_o) and y block size (175 μm ≈ 1.75 λ_o) are marked in Fig. 1f with dotted lines. The corresponding mutual admittance has a positive value, which causes a reduction in the overall radiation impedance of the array, and thus reduces the lasing threshold of the in-phase spatial mode. In Fig. 2e, the far-field beam pattern of a high-order longitudinal DFB mode shows apparent dual lobes. It is evident that different spatial modes can be distinguished from their far-field beam patterns.

Several short-cavity terahertz DFB laser arrays with different cavity length and array grid dimensions were fabricated to verify the effectiveness of the antenna mutual-coupling approach. Scanning electron microscopy (SEM) pictures of the finished devices are shown in Fig. 3. The biasing current is first provided to the laser array through a large bonding pad around the four corners of the laser array and then connected to the whole laser array through the pattern grid. An air-bridge structure is used between the pattern grid and the short-cavity DFB laser to eliminate undesirable current spreading. The laser array is divided into four different quadrants for ease of measurements. Device Chip No. 27 shows narrow single-mode laser emissions from all four quadrants. Each quadrant consists of 37, 28, 31 and 36 identical elements, respectively. The pulsed current–voltage (*I*–*V*) and peak optical power–voltage (*L*–*V*) curves are shown in Fig. 4. Clearly visible lasing 'kinks' are observed from the *I*–*V* curves. From the *L*–*V* curves the dynamic range of the laser array device is far greater than that of the single-element three-section DFB laser, which indicates a reduction in the overall losses of the lasing mode. This change can be attributed to the decrease in radiation losses when adding more elements to an array, as shown in Fig. 2a–c. The spectral measurements show single-mode emissions from all four quadrants near 2.95–2.96 THz. The laser array from quadrant C1 delivers ~6.5 mW pulsed power (in a pulsed mode with a 4% duty cycle) with a maximum slope efficiency of ~450 mW A^{-1}, which is comparable to or even higher than other high-performance DFB lasers in the terahertz range[21–23].

In Fig. 4b, the radiation images were taken by a terahertz camera (model NEC IRV-T0831) with a fast (f-number 3), focal length 100 mm, high-resistivity Si lens in real time at 30 frames per second. To characterize quantitatively the beam divergences, a pyroelectric detector was mounted on a 2D rotational stage ~20 cm away from the surface-emitting laser, scanning between ±30° in both directions without any optics in between the laser and the detector. The lasers were biased at a pulsed mode with a 4% duty cycle and electronically chopped at 100 Hz. In both measurements, narrow and symmetric beam patterns were observed from the laser arrays in all four quadrants. The beam divergence (full-width at half-maximum) was less than 10 × 10° for all cases. Combing the spectral and beam-pattern measurements, it is evident that these subwavelength confined lasers are strongly coupled and form a larger laser array with a single global phase and coherent emission.

Another device, Chip No. 12, which consists of identical three-section DFB lasers as mentioned above but arranged in a Type II grid, shows a quite different behaviour. The lateral distance between adjacent elements is 85 μm (~0.85 λ_o) and the vertical distance is 135 μm (~1.35 λ_o), and they are marked by the dashed lines in Fig. 1g. A comparison of the far-field beam patterns and lasing frequencies between the two laser arrays is shown in Fig. 5. Although the DFB lasers in Chip No. 12 have identical dimensions as the elements in Chip No. 27, the array with the Type II grid (Chip No. 12) lases at a different frequency (~2.825 THz) and the beam pattern has a null line in the centre. From the FEM simulation shown in Fig. 2, this result suggests that the element of the Type II grid laser array is lasing at a different spatial mode. Apparently, the lasing threshold of the fundamental in-phase mode is increased and/or the threshold of the high-order longitudinal mode is decreased under this grid arrangement because of mutual coupling. This is direct evidence that the antenna mutual coupling will modify the threshold of different lasing modes of the laser arrays, and different grid arrangements can be adopted to

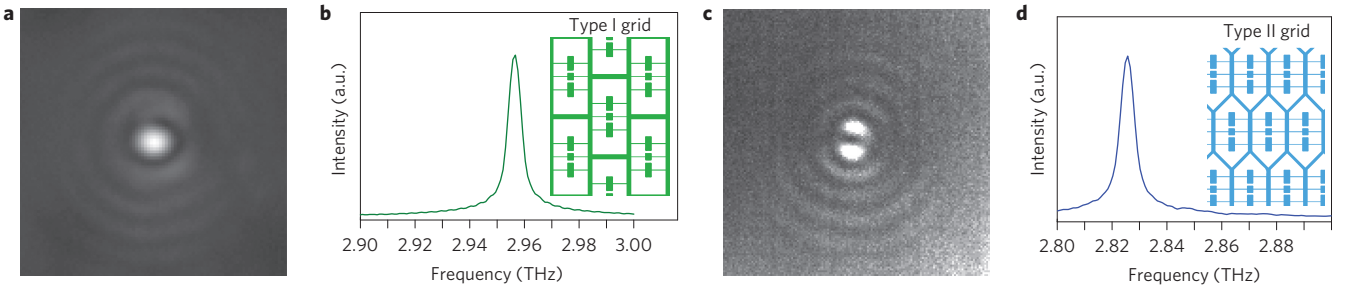

Figure 5 | Type I and Type II grids. a,**b**, Beam patterns (taken by the terahertz camera) (**a**) and emission spectrum (**b**) for the laser array arranged in a Type I grid. **c**,**d**, The same measurements on another coupled laser array arranged in a Type II grid. Although three-section DFB lasers with identical dimensions are used as the building elements in both arrays, the two laser arrays clearly lase in different spectral and spatial modes.

select specific spatial modes. The result is further supported by the mutual admittance simulation shown in Fig. 1g—the corresponding mutual admittance (in the grey dotted circle) under a Type II grid has a small, yet negative, value, which increases the radiation impedance and the lasing threshold of the in-phase spatial mode (with a relative facet polarity of +1, +1, +1, −1, −1, −1) at 3 THz.

Clearly, this new coupling scheme can be applied to other electromagnetic systems with subwavelength elements to achieve a similar reduction in beam divergence and lasing threshold, such as those observed in the square-lattice spaser arrays[24–26]. However, as explained in Dorofeenko *et al.*[27], near-field interaction is the dominant coupling mechanism for self-synchronization in these devices. In essence, the nanoantennas (or holes) in those spaser arrays are part of the cavity, and provide enhanced feedbacks and pumping for lasing actions. However, in the present work, each element in the array is an individual laser that could achieve lasing by itself. The antenna mutual-coupling method is used to phase lock those individual lasers that would otherwise oscillate independently from each other. This method explores the far-field interaction between individual radiation emitters and should lead to stronger and more-stable phase-locking operations. The method presented here could also be applied to arbitrary array arrangement or even compound elements (more than one type of laser element).

In conclusion, a new mechanism based on antenna mutual coupling to achieve global phase locking in a 2D laser array was proposed, verified by numerical simulation and then experimentally demonstrated using subwavelength short-cavity surface-emitting lasers at terahertz frequencies. By changing the total mutual admittance of the laser array through different grid-pattern arrangements, radiation losses that correspond to specific spatial modes can be enhanced or suppressed. A simplified numerical method was developed to evaluate quickly this mutual-coupling strength for different array grid patterns, which allows a fast optimization of grid dimensions to achieve robust phase-locked operations. More than 37 laser elements—the highest number ever reported at this frequency—are phase locked to each other. The array spans over ~8 λ_o and delivers up to 6.5 mW of single-mode pulsed power (4% duty cycle) at ~3 THz. The typical beam divergence is $<10 \times 10°$, which is close to the diffraction limit by the size of each quadrant (~800×800 μm at a wavelength of 100 μm). Clearly, the far-field nature of this phase-locking mechanism allows scalability to even larger arrays, which enables the achievement of highly tight beam patterns. As electromagnetic waves are scalable, the result presented here can be applied to other frequency ranges by scaling the dimensions.

Methods

Methods and any associated references are available in the online version of the paper.

Received 18 December 2015; accepted 27 April 2016; published online 13 June 2016

References

1. Hill, M. T. *et al.* Lasing in metallic-coated nanocavities. *Nature Photon.* **1,** 589–594 (2007).
2. Noginov, M. A. *et al.* Demonstration of a spaser-based nanolaser. *Nature* **460,** 1110–1112 (2009).
3. Oulton, R. F. *et al.* Plasmon lasers at deep subwavelength scale. *Nature* **461,** 629–632 (2009).
4. Zhang, J. P. *et al.* Photonic-wire laser. *Phys. Rev. Lett.* **75,** 2678–2681 (1995).
5. Hill, M. T. & Gather, M. C. Advances in small lasers. *Nature Photon.* **8,** 908–918 (2014).
6. Ackley, D. E. Single longitudinal mode operation of high power multiple-stripe injection lasers. *Appl. Phys. Lett.* **42,** 152–154 (1983).
7. Katz, J., Maargalit, S. & Yariv, A. Diffraction coupled phase-locked semiconductor laser array. *Appl. Phys. Lett.* **42,** 554–556 (1983).
8. Brunner, D. & Fischer, I. Reconfigurable semiconductor laser networks based on diffractive coupling. *Opt. Lett.* **40,** 3854–3857 (2015).
9. Chen, K. L. & Wang, S. Single-lobe symmetric coupled laser arrays. *Electron. Lett.* **21,** 347–349 (1985).
10. Streifer, W., Welch, D., Cross, P. & Scifres, D. Y-junction semiconductor laser arrays. Part I—theory. *IEEE J. Quantum Electron.* **23,** 744–751 (1987).
11. Botez, D. & Peterson, G. Modes of phase-locked diode-laser arrays of closely spaced antiguides. *Electron. Lett.* **24,** 1042–1044 (1988).
12. Botez, D. High-power monolithic phase-locked arrays of antiguided semiconductor diode lasers. *IEE Proc. J.* **139,** 14–23 (1992).
13. Kao, T.-Y., Hu, Q. & Reno, J. L. Phase-locked arrays of surface-emitting terahertz quantum-cascade lasers. *Appl. Phys. Lett.* **96,** 101106 (2010).
14. Orlova, E. E. *et al.* Antenna model for wire lasers. *Phys. Rev. Lett.* **96,** 173904 (2006).
15. Faist, J. *et al.* Quantum cascade laser. *Science* **264,** 553–556 (1994).
16. Kohler, R. *et al.* Terahertz semiconductor heterostructure laser. *Nature* **417,** 156–159 (2002).
17. Kumar, S. *et al.* Surface-emitting distributed feedback terahertz quantum-cascade lasers in metal–metal waveguides. *Opt. Express* **15,** 113–128 (2007).
18. Williams, B. S., Kumar, S., Callebaut, H., Hu, Q. & Reno, J. L. Terahertz quantum-cascade laser at $\lambda \approx 100$ μm using metal waveguide for mode confinement. *Appl. Phys. Lett.* **83,** 2124–2126 (2003).
19. Balanis, C. A. *Antenna Theory: Analysis and Design* (John Wiley & Sons, 2012).
20. Derneryd, A. G. A theoretical investigation of the rectangular microstrip antenna element. *IEEE Trans. Antennas Propag.* **26,** 532–535 (1978).
21. Amanti, M. I., Fischer, M., Scalari, G., Beck, M. & Faist, J. Low-divergence single-mode terahertz quantum cascade laser. *Nature Photon.* **3,** 586–590 (2009).
22. Xu, G. *et al.* Efficient power extraction in surface-emitting semiconductor lasers using graded photonic heterostructures. *Nature Commun.* **3,** 952 (2012).
23. Kao, T.-Y., Cai, X., Lee, A. W., Reno, J. L. & Hu, Q. Antenna coupled photonic wire lasers. *Opt. Express* **23,** 17091–17100 (2015).
24. van Beijnum, F. *et al.* Surface plasmon lasing observed in metal hole arrays. *Phys. Rev. Lett.* **110,** 206802 (2013).
25. Zhou, W. *et al.* Lasing action in strongly coupled plasmonic nanocavity arrays. *Nature Nanotech.* **8,** 506–511 (2013).
26. Zhang, C. *et al.* Plasmonic lasing of nanocavity embedding in metallic nanoantenna array. *Nano Lett.* **15,** 1382–1387 (2015).
27. Dorofeenko, A. V. *et al.* Steady state superradiance of a 2D-spaser array. *Opt. Express* **21,** 14539–14547 (2013).
28. Li, S., Witjaksono, G., Macomber, S. & Botez, D. Analysis of surface-emitting second-order distributed feedback lasers with central grating phaseshift. *IEEE J. Sel. Top. Quantum Electron.* **9,** 1153–1165 (2003).

Acknowledgements

This work is supported by the National Aeronautics and Space Administration and National Science Foundation, and also performed at the Center for Integrated Nanotechnologies, a US Department of Energy, Office of Basic Energy Sciences user facility. Sandia National

Laboratories is a multiprogram laboratory operated by Sandia Corporation, a wholly owned subsidiary of Lockheed Martin Corporation, for the US Department of Energy's National Nuclear Security Administration under contract DE-AC04-94AL85000.

Author contributions

T.-Y.K. conceived the strategy, designed and fabricated the antenna mutual coupled laser arrays and performed the measurements and analysis, and J.L.R. provided the material growth. All the work was done under the supervision of Q.H.

Additional information

Supplementary information is available in the online version of the paper. Reprints and permissions information is available online at www.nature.com/reprints. Correspondence and requests for materials should be addressed to Q.H.

Competing financial interests

The authors declare no competing financial interests.

Methods

FEM simulation. Using 3D FEM simulation, quasi-eigenmodes of the whole antenna-coupled laser structures can be found with detailed information of both the electric and magnetic field distributions. From the eigenfrequencies and the corresponding radiation losses we can estimate the lasing frequency and calculate far-field beam patterns. The simulations were carried out using COMSOL Multiphysics version 4.3. No metal losses and material losses were taken into account when performing the 'cold cavity' eigenmode simulation. The simulation environment was surrounded with a perfect-matching layer to absorb unphysical reflections from the boundaries.

***L–I–V* and spectral measurements.** For pulsed *L–I–V* measurements, the lasers were operated at 20 kHz with a 400 ns pulse duration (0.8% duty cycle) at a temperature of 10 K. The optical power was measured with a liquid-helium-cooled Ge:Ga photodetector. Spectra were measured using a Fourier transform infrared spectrometer (FTIR; model Thermo Nicolet 6700) with a liquid-helium-cooled Ge:Ga photodetector as the external detector.

Power measurements. Power was measured without any focusing optics between the laser and the power meter except a high-density polyethylene window on the cryostat. Pulsed measurements were performed using a Thomas Keating absolute terahertz power meter at a 30 Hz electronic chopping frequency. The laser under test was operated at 100 kHz with a 400 ns pulse duration (4% duty cycle) at a temperature of 10–12 K inside a Cryomech Pulse tube cryorefrigerator (model PT 810). All the power measurements were done in the atmosphere without purging.

Beam-pattern measurements. Far-field beam patterns were measured with a pyroelectric detector mounted on a 2D motorized scanning stage, which was placed at 20 cm from the surface-emitting laser, scanning between ±30° in both directions without any optics between the laser and the detector. The laser was operated near the peak power in a pulsed mode with a 4% duty cycle and electronically chopped at 100 Hz.

Near-infrared and terahertz imaging. The images were taken with a NEC THz camera (model IRV-T0831) with a fast (f-number 3), 100-mm high-resistivity Si lens in real time at 30 frames per second.

nature photonics

SUPPLEMENTARY INFORMATION

DOI: 10.1038/NPHOTON.2016.104

Phase-locked laser arrays through global antenna mutual coupling

Tsung-Yu Kao[1,2], John L. Reno[3], and Qing Hu[1]

[1]Department of Electrical Engineering and Computer Science and Research Laboratory of Electronics, Massachusetts Institute of Technology, Cambridge, MA 02139, USA

[2]LongWave Photonics L.L.C., Mountain View, CA 94043, USA

[3]Sandia National Laboratories, Center of Integrated Nanotechnologies, MS 1303, Albuquerque, NM 87185-130, USA

Implicit Assumptions in Calculating G_{sum}, and G_{grid}

In calculating the total mutual admittance G_{sum} as defined in equation (2), we implicitly assume that G_{sum} of the system follows the simple addition rule by summing the mutual admittances between subsystems. Note that, in this equation, the coupling between slot antennas pair within the same DFB laser is not taken into account toward the total mutual admittances of the system, as they are within the same laser cavity and therefore have definite phase and amplitude relations. When a 3-section second-order DFB laser operates at the desired fundamental surface-emitting mode, the polarity relationship between slot facets can be described as (+1, +1, +1, −1, −1, −1), as depicted in Fig. 1c in the main manuscript. The change in polarity sign is the desired outcome of the center π shift, which is introduced to obtain single-lobe beam patterns from the surface-emitting laser [1]. Again, for

DOI: 10.1038/NPHOTON.2016.104

simplicity, we assume the amplitude of each slot aperture to be identical for the surface-emitting mode. Thus A_i = 1, 1, 1, −1, −1, −1 for i = 1-6.

In calculating $\boldsymbol{G_{grid}}$, for simplicity only contributions from nearest neighbors are included. Although the contribution in G_{grid} is still not negligible when the distance between two DFB elements is larger than a few wavelengths, in our numerical model, the contribution from the nearest neighbor is sufficiently strong to illustrate the concept of this new coupling mechanism.

It is worth pointing out that, the numerical method presented here is only valid for estimating the strength of mutual coupling once the electric field distributions for all slot facets (A_{ij}) and the phase and magnitude relationship between array elements (B_k) are given. Full-wave electromagnetic simulations as shown in the main manuscript are still needed for more rigorous result.

Fabrication Method

Due to uncertainties in fabrication, a series of short-cavity THz DFB laser with different cavity length, gap size, and different array grid dimensions are fabricated on a single wafer. The designs are mainly consisted of 3-section short-cavity DFB lasers with two different array structures, offset rectangular (Type I) and hexagonal (Type II). After preforming the standard Au-Au wafer-bonding process used in THz QC lasers and removing the residue substrate to expose the active medium by wet etching in citric acid, a thin SiO_2 layer is blankly deposited on the wafer and then patterned to provide electrical isolation for the bonding pad. Standard contact lithography with image reversal

photoresist AZ 5214 is then used to form Ti/Au metal mask on top of the active region. Area that is not masked by the Ti/Au pattern is then etched using inductive coupled plasma reactive ion etcher (ICP-RIE) in $SiCl_4$ chemistry until the bottom metal plane is reached. A wet etch step using NH_4OH solution is then used to remove the semiconductor material beneath the thin contact fin to form the air bridge structure. Total 18 different laser array designs, each with 2.5 × 2.5 mm in size, are fabricated together as a whole wafer and then die sawed into sub-chips for testing.

The active gain medium is based on molecular beam epitaxy (MBE) grown GaAs/$Ga_{0.85}Al_{0.15}As$ multiple quantum well structure. The thickness of the gain medium is 10 μm, based on the design OWI-180E [2] (a 3-well resonant-phonon design, wafer number VB0205).

Preliminary Test of Surface-Emitting Laser with Different Element Numbers

Before designing the mutual coupled laser array, a series of single-element second-order DFB lasers with different grating sections (a center π-shifter and even numbers of 2^{nd}-order DFB grating periods) are first fabricated and tested using the same gain medium. The normalized *I-V* curves are shown on the following Fig. S1. From 3- to 9-section devices, the current densities and the biasing voltages of the DFB lasers match well with each other except near the lasing thresholds. The lasing thresholds of 7- and 9-section devices are almost identical, while the 5-section device shows a small increase in lasing threshold. The lasing threshold of the 3-section device is substantially increased. The corresponding reduction in dynamic range is also obvious in this figure. This is strong evidence that the total loss of the 3-section DFB laser is near, but still below the

DOI: 10.1038/NPHOTON.2016.104

maximum material gain of the gain medium. 3-section DFB laser at ~3 THz typically has 15-μm in width, and ~30-40 μm in total laser length, which is much smaller than the wavelength in the free space (~100 μm).

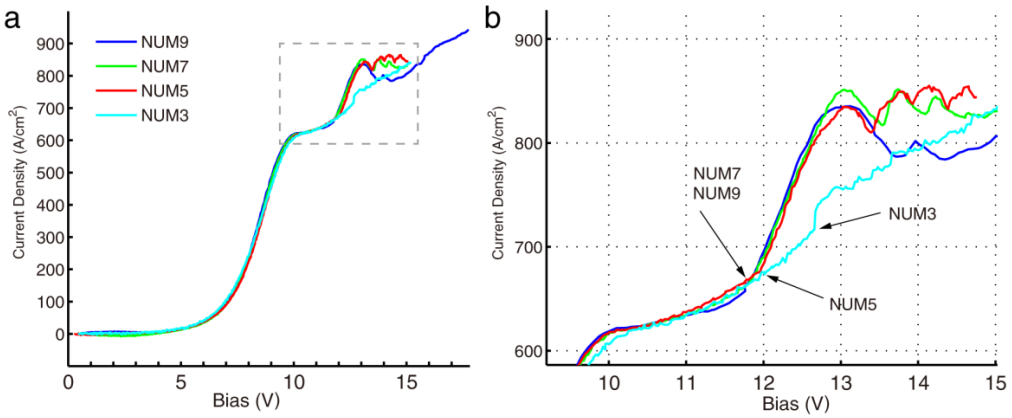

Figure S1: **a.** Pulsed *I-V* curves at 10 K of a series of single-element second-order DFB lasers with different sections. **b.** Zoom-in version of the same *I-V* curves. The lasing kinks of different devices are also marked.

Descriptions of Devices under Test:

The laser array show global mutual coupling effect—Device Chip #27 (Label: 3THZ_R15_P3X+H-R)—is consisted of 3-section DFB lasers with 15-μm ridge width and 16.5-μm center cavity length which are arranged in an offset rectangular grid. The lateral distance between adjacent elements (*xblock* size) is 85 μm (~0.85λ_o) and the vertical distance (*yblock* size) is 175 μm (~1.75λ_o). This laser array is divided into four parts with upper right, lower right, lower left, and upper left corner (marked as C1 to C4). Each quadrant is consisted of 37, 28, 31, and 36 identical elements, respectively. The slight difference in numbers of elements in each quadrant is due to grid pattern geometry.

The pulsed maximum operating temperature T_{max} of the laser array is increased from 45 K (single element) to 80–90 K (28–37 elements). The overall THz DFB laser array has a maximum operating temperature T_{max} of 80 K (pulsed) and 47 K (c.w.). Quadrant C1 delivers 6.5 mW single-mode pulsed power when biased at 4% duty-cycle at 10 K.

Coupling Between Multiple Quadrats:

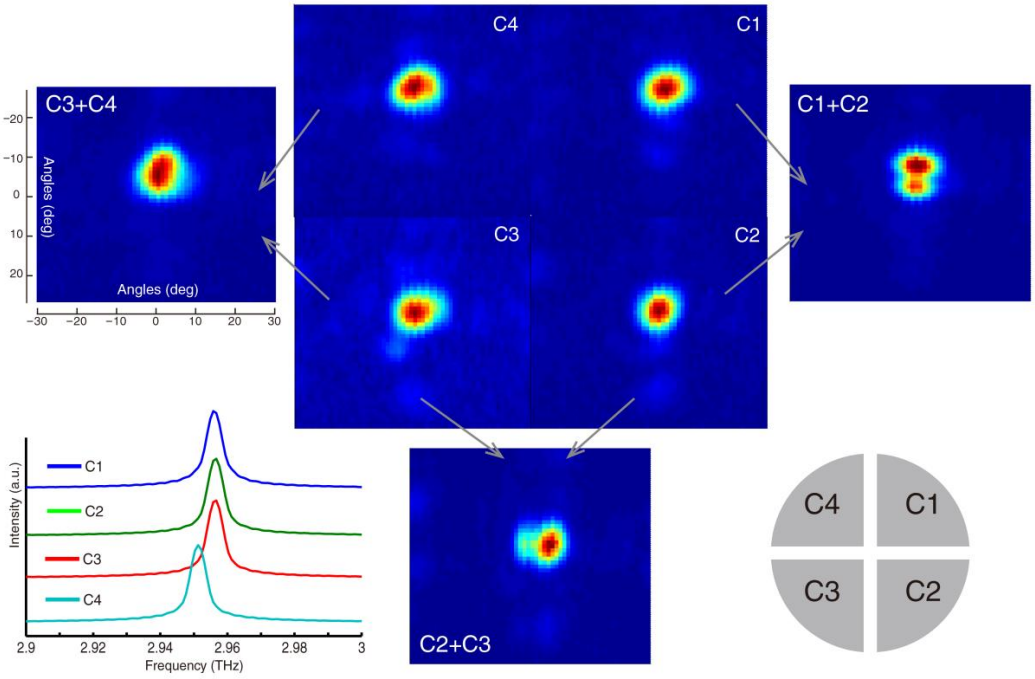

Figure S2: Far-field beam pattern for different array quadrant combinations.

More than one quadrant of the laser array can be biased at the same time. The beam patterns from different combinations (C1+C2, C2+C3, and C3+C4) are shown in the figure. Although beam pattern from combination C1+C2 is not single-lobe, it shows two narrower beam spots with a null in the center. Apparently lasers from C1 and C2

DOI: 10.1038/NPHOTON.2016.104

form a larger coupled laser arrays since the beam of each lobe is tighter along the vertical direction. Better beam patterns can be observed when C2 and C3 are biased by the same pulse source. Now the beam pattern of the main lobe is tighter along the lateral direction with a clear single lobe. Note that part of the radiation energy is presented outside the main lobe and might be contributed to the non-perfect timing between biasing current pulses. Due to the nature of pulsed operation, it is challenging to keep the biasing pulse arriving at two separated laser arrays simultaneously. We speculate that this timing offset could destroy the phase-locking operation, leading to partial phase-locking. Combinations of C3+C4 is also shown here. Since C3 and C4 are lasing at distinctively different frequencies (see spectra in the same figure) and thus cannot be easily phase-locked, no beam narrowing effect is observed. When we designed the layout of C1-C4, we did not aim to achieve phase-locking between those arrays. The unintended results of partial phase locking indicate that even global phase-locking between arrays can be achieved in properly designed structures.

Laser Array Design Method:

When choosing the building element of a laser array, it is important to keep the losses of the high-order lateral and longitudinal modes near the desired lasing mode under control. This task is usually achieved through several different approaches: 1) place the element cavity lasing mode around the peak gain frequency of the gain medium, 2) increase the frequency spacing between modes by reducing the length the DFB laser

element, and 3) increase the difference in lasing thresholds between desired and unwanted lasing modes through a careful cavity design.

Fig. S3 (a) shows the plot of gain threshold versus frequency for a 3-section second-order DFB laser from FEM simulation. The estimated gain spectrum of the gain medium used in this work is also plotted in shaded region. Magnetic field distributions for modes in the laser cavity with the first 6 lowest radiation losses are shown in part (b). Evidently, mode B is the desired surface-emitting mode with a single-lobe far-field beam pattern, mode A is the 2^{nd}-order longitudinal mode, and mode C-F are high-order lateral modes.

As described in the aforementioned approaches, frequency of mode B is designed to be near the gain peak and by choosing a 3-period laser cavity, the frequency spacing between mode A and B (roughly 150 GHz) provides further protection so that mode A is sufficiently away from the gain peak in addition that mode A having a higher threshold. For mode C and D, the radiation losses are already higher than mode B. Although mode E, F have lower radiation losses than the desired lasing mode B, their eigenfrequencies are so far from the gain peak that the laser would never lase at these modes. It is also worth pointing out that the confinement factor Γ and the material losses from semiconductor and metal are not included in the FEM simulation. If included, the high-order lateral modes often see lower confinement factor and higher material loss from metal and surface roughness. Both effects further increase the lasing threshold for these modes, providing even greater mode discrimination against the undesired mode.

DOI: 10.1038/NPHOTON.2016.104

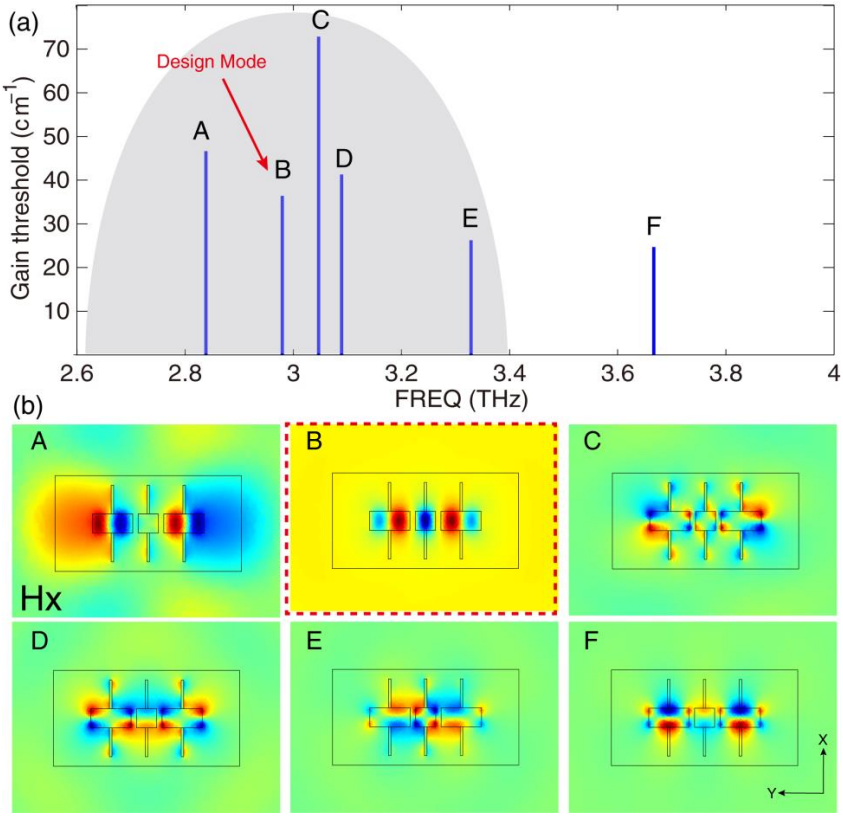

Figure S3. (a) Gain threshold versus frequency plot for a 3-period second-order DFB laser. The estimated gain spectrum of the gain medium used in this work is also plotted in the shaded region. (b) Magnetic field distribution for 6 different modes of the DFB laser.

Once the dimensions of the laser element are decided, phase and amplitude information on each facet on the laser element can be extracted from the FEM simulation as depicted in Fig.1c in the main manuscript and mutual conductance calculation between two laser elements at different spacing can be plotted (Fig 1e). Fig 1f and 1g can be treated as graphical tools to quickly identify grid spacing (xblock, yblock) which could enhance or reduce radiation losses of the in-phase supermode under different type of grid arrangement.

While plots in Fig 1 provide the conceptual tool to understand the effect of mutual coupling in a laser array, several simplifying assumptions and approximations are made (see Supplementary Information—"Implicit Assumptions in Calculating G_{sum} , and G_{grid}"). In order to take into account all the possible supermodes and their losses in the array simultaneously without any *a priori* assumptions, a series of 3D full-wave FEM quasi-eigenmode simulations were carried out for laser array with different numbers of elements around desired grid spacing (xblock, yblock) and verify that the in-phase supermode has the lowest threshold among all spatial modes, and thus it will be the lasing mode. Considering fabrication limitation and space requirement by the bias network, we choose grid spacing (0.85λ, 1.75λ) for Type I grid as marked on Fig 1f to demonstrate the in-phase laser array.

Reference:

1. Li, S. et al. Analysis of surface-emitting second-order distributed feedback lasers with central grating phaseshift. *IEEE J. Sel. Topics Quantum Electron* **9**, 1153 (2003).
2. Kumar, S. et al. Low-threshold Terahertz quantum-cascade lasers with one-well injector operating up to 174 K. *Conference on Quantum electronics and Laser Science Conference (CLEO)*. (2009).